Review

Theory of Photoinduced Phase Transitions in Molecular Conductors: Interplay Between Correlated Electrons, Lattice Phonons and Molecular Vibrations

Kenji Yonemitsu [1,2,3]

[1] Institute for Molecular Science, Okazaki, Aichi 444-8585, Japan; E-Mail: kxy@ims.ac.jp;
  Tel.: +81-564-55-7312; Fax: +81-564-53-4660.

[2] Department of Functional Molecular Science, Graduate University for Advanced Studies, Okazaki,
  Aichi 444-8585, Japan

[3] JST, CREST, Tokyo 102-0076, Japan

Abstract: Dynamics of photoinduced phase transitions in molecular conductors are reviewed from the perspective of interplay between correlated electrons and phonons. (1) The charge-transfer complex TTF-CA shows a transition from a neutral paraelectric phase to an ionic ferroelectric phase. Lattice phonons promote this photoinduced transition by preparing short-range lattice dimerization as a precursor. Molecular vibrations stabilize the neutral phase so that the ionic phase, when realized, possesses a large ionicity and the Mott character; (2) The organic salts θ-(BEDT-TTF)$_2$RbZn(SCN)$_4$ and α-(BEDT-TTF)$_2$I$_3$ show transitions from a charge-ordered insulator to a metal. Lattice phonons make this photoinduced transition hard for the former salt only. Molecular vibrations interfere with intermolecular transfers of correlated electrons at an early stage; (3) The organic salt κ-(d-BEDT-TTF)$_2$Cu[N(CN)$_2$]Br shows a transition from a Mott insulator to a metal. Lattice phonons modulating intradimer transfer integrals enable photoexcitation-energy-dependent transition pathways through weakening of effective interaction and through introduction of carriers.

Keywords: photoinduced phase transition; neutral-ionic transition; charge-order melting; metal-insulator transition

1. Introduction

Most of organic conductors are now recognized as strongly correlated electron systems, which show a variety of electronic phases depending on temperature T, pressure P, constituent elements, *etc*. In order to pursue further possibilities of organic conductors, the feasibility of manipulating the electronic phases on designed spatial and temporal scales is important. Phase transitions are induced in equilibrium by the variation of parameters such as T and P. They can be photoinduced, under nonequilibrium environment, on different time scales ranging from femtoseconds to nanoseconds.

Photoinduced phase transitions are not limited to molecular conductors. However, molecular systems constitute an important class of materials, the dynamic characteristics of which are well investigated both experimentally and theoretically. So, let us summarize the characteristics of their electronic properties. First of all, electric conduction is realized by an overlap between neighboring (highest occupied or lowest unoccupied) molecular orbitals, so that the stacking structure of molecules is important. The overlap is usually confined in particular directions, so that the electric conduction is limited to low-dimensional space. As is well known in condensed matter physics, the instability of the Fermi sea becomes stronger as the spatial dimension becomes lower. Thus, a tendency to form a long-range order, making the system an insulator or a superconductor, is strengthened. Organic conductors can then possess a variety of electronic phases. In some cases, the dimensionality is continuously tuned by changing T, P, and constituent elements [1–3]. Furthermore, in quasi-two-dimensional molecular conductors, molecular arrangements are continuously changed from squares to triangles, namely, geometric frustration is tuned to modify the phase diagram itself [4,5].

Secondly, molecules, the building blocks of molecular conductors, are large objects and the intermolecular overlaps are generally small, so that the ratios of on-site Coulomb energies to the transfer integrals are large compared with those in transition-metal oxides. This makes electrons correlated strongly with each other. The highest occupied or lowest unoccupied molecular orbitals generally have many nodes, so that the transfer integrals are sensitive to the intermolecular distance and the relative orientation. This makes electrons to couple strongly with lattice phonons. Molecules themselves are soft and the molecular orbitals are sensitive to the bond lengths inside them. This makes electrons to couple strongly with molecular vibrations. Furthermore, these interaction strengths are comparable, which causes the variety of the electronic phases realized in molecular conductors.

¿From the viewpoint of manipulating the electronic phases under nonequilibrium environment, various degrees of cooperativity derived from these interactions are important. Photoinduced phase transitions take advantage of such cooperativity. They have been realized first in molecular materials and are now in other materials including transition metal oxides and assembled metal complexes [6–8]. Even now, their study in molecular conductors is well advanced with regard to the variety of transitions, the time resolution of experiments, theoretical understandings, *etc*. Photoinduced phase transitions that are realized experimentally and simulated theoretically, including transitions from Mott insulator to metal phases in halogen-bridged transition-metal-chain compounds [9,10], quasi-one- [11–14] and two-dimensional [15,16] organic salts, charge-ordered insulator to metal phases in quasi-one- [17,18] and two-dimensional [19–22] systems, charge-density-wave to charge-polarization phases [23,24],

ferroelectric ionic to paraelectric neutral phases [25,26], neutral to ionic phases [27,28] and nonmagnetic to paramagnetic phases [29–32].

As for time evolutions studied theoretically, long-term stochastic evolutions of statistically averaged quantities were treated by master equations [33]. Meanwhile, short-term deterministic evolutions of wave functions are treated by the time-dependent Schrödinger equation. Different approximations are introduced to treat wave functions. As the time scale is shortened, electron correlations become important and need to be treated more exactly, as well as the quantum nature of phonons, so that the dimensions of the wave function and the evolution operator are increased in an exponential manner with respect to the system size. Quite recently, with a time resolution of 10 fs, electronic motion and its interference with molecular vibrations have been observed [22]. Coherent control of electronic phases may be realized in some molecular material in the near future.

In order to take full advantage of the characteristics of molecular conductors, intramolecular or intradimer degrees of freedom should be exploited. Thanks to the improved time resolution, the evolution of electronic spectra modulated by molecular vibrations is clarified, which gives us information about how the ground state is stabilized by the electron-molecular-vibration couplings [22,27,28]. Intramolecular or intradimer degrees of freedom may produce different transition pathways depending on the way by which the system is photoexcited. For instance, the use of molecular degrees of freedom inside a dimer in dimer-Mott insulators enables photoinduced insulator-to-metal transitions through the weakening of effective interaction and the introduction of carriers [15,16]. The existence of at least two hierarchies consisting of intra- and inter-molecular degrees of freedom will become a central issue for relaxation processes required for photoinduced phase transitions.

In this context, from the perspective of interplay between intra- and inter-molecular degrees of freedom and interplay among correlated electrons, lattice phonons and molecular vibrations, we review the following photoinduced phase transitions realized in molecular conductors. (1) The photoinduced neutral-to-ionic transition in the mixed-stack charge-transfer complex tetrathiafulvalene-p-chloranil (TTF-CA) is from a paraelectric phase to a ferroelectric phase, and basically from a band insulator to a Mott insulator. It is shown that, in order for the ionic phase to be a typical Mott insulator, electron-molecular-vibration couplings need to be large, stabilizing the neutral phase, which is counterintuitive in the sense that the neutral phase is a band insulator. Lattice phonons are responsible for dimerization and consequently for the ferroelectric ground state. Above the neutral-ionic transition temperature, dimerization is short-range, but it promotes the photoinduced growth of a dimerized ionic domain as a seed; (2) The charge orders in the organic salts θ-(BEDT-TTF)$_2$RbZn(SCN)$_4$ and α-(BEDT-TTF)$_2$I$_3$ [BEDT-TTF=bis(ethylenedithio)tetrathiafulvalene] both show a horizontal-stripe pattern and are quite similar. Their photoinduced dynamics are, however, quite different. It is shown that their slightly different crystal structures make the effects of electron-lattice couplings quite different, because the way by which the charge order is stabilized is different, in spite of the fact that the charge order is basically stabilized by Coulomb interactions. At an early stage, collective motion of electron transfers is observed and it interferes with molecular vibrations; (3) The Mott insulator phase in κ-(d-BEDT-TTF)$_2$Cu[N(CN)$_2$]Br can be converted into a metallic phase by photoexcitation. In general, this transition is induced by the weakening of effective interaction relative to the bandwidth or the introduction of carriers away from half filling. Both transition pathways are realized by tuning the

energy of photoexcitation, using intradimer and interdimer charge-transfer excitations in the dimer-Mott insulator phase.

2. Neutral-Ionic Transition in TTF-CA

For TTF-CA, dimerization is essential to the ferroelectric ground state in the ionic phase. To explain the dimerization, different types of electron-lattice couplings have been employed [34–37]. Lattice modulation of transfer integrals triggers the spin-Peierls mechanism for dimerization [34,36,37], while lattice modulation of Coulomb interaction strengths can also cause dimerization [35]. Photoinduced neutral-to-ionic transition dynamics has been calculated on the basis of the latter mechanism [38]. However, it cannot reproduce the quick growth and oscillation of the lattice dimerization experimentally observed after photoexcitation [27]. Therefore, we use a model based on the former mechanism. It is noted that the long-range Coulomb interaction is important for the experimentally observed [39], coherent motion of a macroscopic neutral-ionic domain boundary [26].
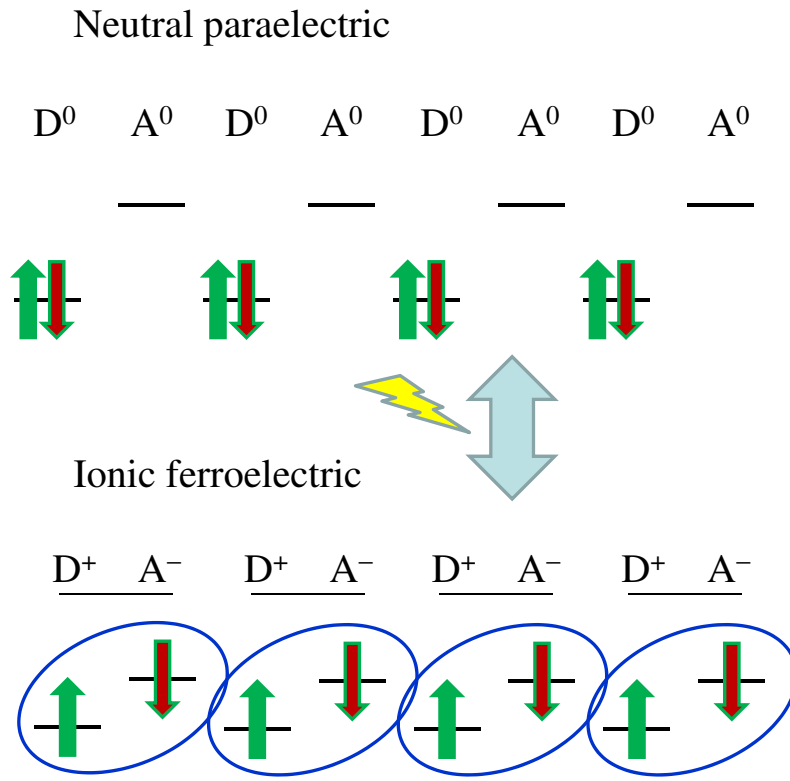
The one-dimensional half-filled extended ionic Peierls–Holstein–Hubbard model used here is written as

$$
\begin{aligned}
H = &- \sum_{j\sigma}[t_0 - \alpha(u_{j+1} - u_j)](c_{j\sigma}^\dagger c_{j+1\sigma} + c_{j+1\sigma}^\dagger c_{j\sigma}) - \sum_{mj\sigma} \beta_j^{(m)} v_j^{(m)} c_{j\sigma}^\dagger c_{j\sigma} \\
&+ \frac{\Delta}{2} \sum_{j\sigma}(-1)^j c_{j\sigma}^\dagger c_{j\sigma} + U \sum_j n_{j\uparrow} n_{j\downarrow} + V \sum_j n_j n_{j+1} \\
&+ \sum_j \left[\frac{K_\alpha}{2}(u_{j+1} - u_j)^2 + \frac{2K_\alpha}{\omega_\alpha^2} \dot{u}_j^2 \right] + \sum_{mj} \left[\frac{K_{\beta j}^{(m)}}{2} v_j^{(m)2} + \frac{K_{\beta j}^{(m)}}{2\omega_{\beta j}^{(m)2}} \dot{v}_j^{(m)2} \right]
\end{aligned}
\tag{1}
$$

where $c_{j\sigma}^\dagger$ creates an electron with spin σ at site j, $n_{j\sigma} = c_{j\sigma}^\dagger c_{j\sigma}$, and $n_j = \sum_\sigma n_{j\sigma}$. The parameter t_0 denotes the transfer integral on a regular lattice, Δ the site energy difference between neighboring orbitals when molecular distortions are absent, U the on-site repulsion strength, and V the nearest-neighbor repulsion strength. The lattice displacement u_j at site j modulates the transfer integral between the $(j-1)$th and jth orbitals and that between the jth and $(j+1)$th orbitals with the coefficient $\mp\alpha$. The displacement $v_j^{(m)}$ in the mth mode on the jth molecule modulates the site energy with the coefficient $\beta_j^{(m)}$. The quantities $\dot{u}_j$ and $\dot{v}_j^{(m)}$ are the time derivatives of u_j and $v_j^{(m)}$, respectively. The parameters K_α and $K_{\beta j}^{(m)}$ are their elastic coefficients, and ω_α and $\omega_{\beta j}^{(m)}$ are their bare phonon energies, respectively.

For the model parameters, we take eV as the unit of energy and use $t_0 = 0.17$, $U = 1.5$, and $V = 0.6$; we vary Δ around the boundary between the neutral and ionic phases shown in Figure 1.

Figure 1. Schematic electronic and lattice structures of TTF-CA. Photoexcitation creates transient ionicity.

We define the strengths of these couplings as $\lambda_\alpha \equiv \alpha^2/K_\alpha$ and $\lambda_{\beta j} \equiv \sum_m \beta_j^{(m)2}/K_{\beta j}^{(m)}$. The displacements are scaled using $\alpha = \beta_j^{(m)} = 1$. For simplicity, we set $\lambda_{\beta 2i-1} = \lambda_{\beta 2i} = \lambda_\beta$. As for phonons, we take one mode for the donor molecule and two modes for the acceptor molecule in addition to the lattice phonon mode, and use parameters that approximately reproduce the experimentally observed phonon energies [27]: $\omega_\alpha = 0.013$, $\omega_{\beta 2i}^{(1)} \equiv \omega_{\beta A1} = 0.040$, $\omega_{\beta 2i-1}^{(1)} \equiv \omega_{\beta D} = 0.055$, and $\omega_{\beta 2i}^{(2)} \equiv \omega_{\beta A2} = 0.12$. Donor and acceptor molecules are specified by odd and even j's, respectively. For simplicity, we set $K_{\beta 2i}^{(1)} = K_{\beta 2i}^{(2)}$.

Photoexcitation is introduced through the Peierls phase

$$c_{i\sigma}^\dagger c_{j\sigma} \rightarrow e^{(ie/\hbar c)(j-i)A(t)} c_{i\sigma}^\dagger c_{j\sigma} \tag{2}$$

The time-dependent vector potential $A(t)$ for a pulse of an oscillating electric field is given by

$$A(t) = \frac{F}{\omega_{\mathrm{pmp}}} \cos(\omega_{\mathrm{pmp}} t) \frac{1}{\sqrt{2\pi} T_{\mathrm{pmp}}} \exp\left(-\frac{t^2}{2T_{\mathrm{pmp}}^2}\right) \tag{3}$$
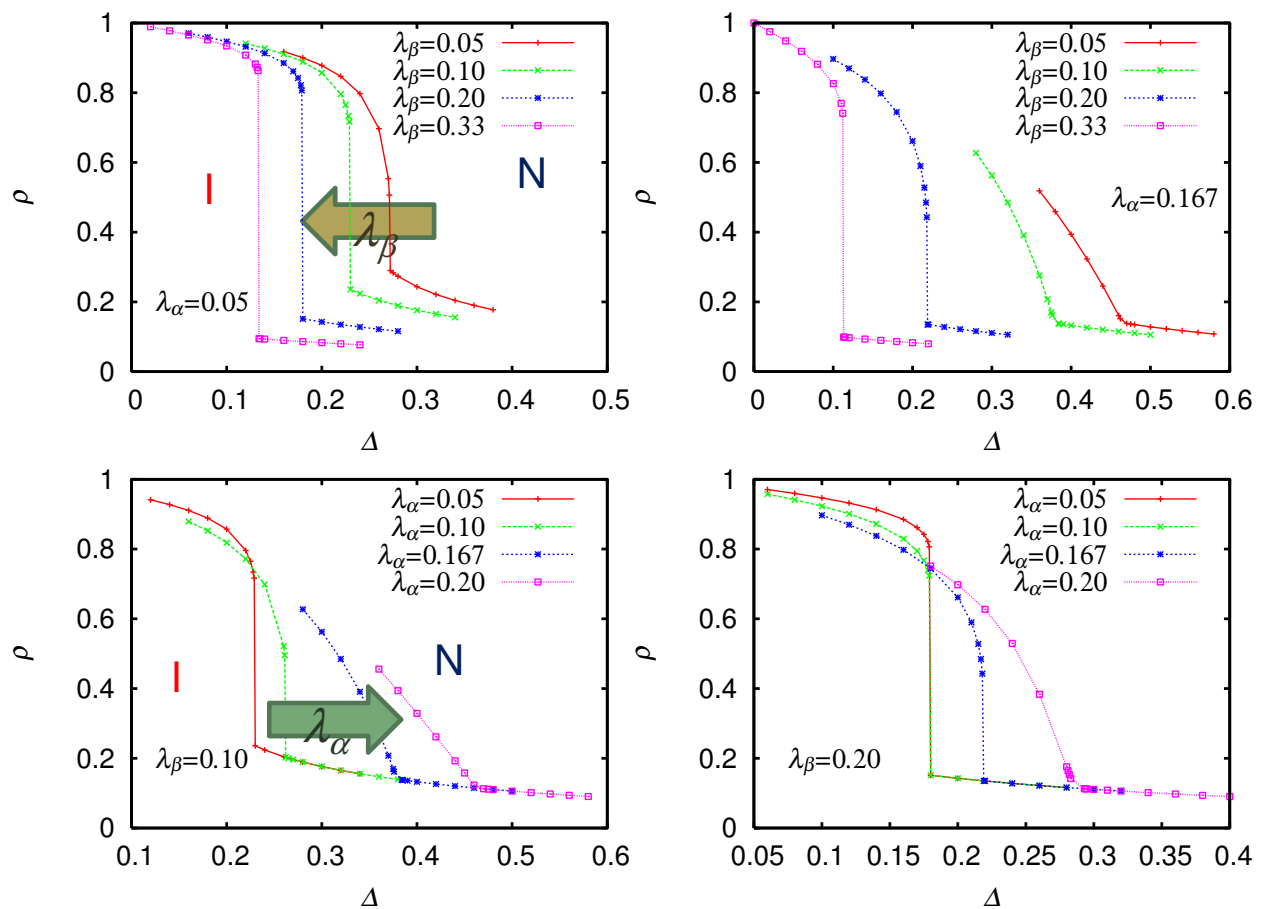
where ω_{pmp} is the excitation energy, T_{pmp} is the pulse width, and F is the electric field amplitude. The time-dependent Schrödinger equation for the exact many-electron wave function on the chain of $N = 12$ sites with periodic boundary condition is numerically solved by expanding the exponential evolution operator with a time slice $dt = 0.02$ eV^{-1} to the 15th order and by checking the conservation of the norm [13]. The initial state is set in the electronic ground state. The classical equations for the lattice and molecular displacements are solved by the leapfrog method, where the forces are derived from the Hellmann–Feynman theorem.

Figure 2 shows the ionicity

$$\rho \equiv 1 + (1/N) \sum_{j=1}^{N} (-1)^j \langle n_j \rangle \qquad (4)$$

as a function of the site energy difference Δ near the phase boundary with different combinations of λ_α and λ_β.

Figure 2. Ionicity ρ as a function of site energy difference Δ for weak Peierls coupling $\lambda_\alpha = 0.05$ (upper left), strong Peierls coupling $\lambda_\alpha = 0.167$ (upper right), weak Holstein coupling $\lambda_\beta = 0.10$ (lower left), and strong Holstein coupling $\lambda_\beta = 0.20$ (lower right). From [28]. Reproduced with permission from JPSJ.
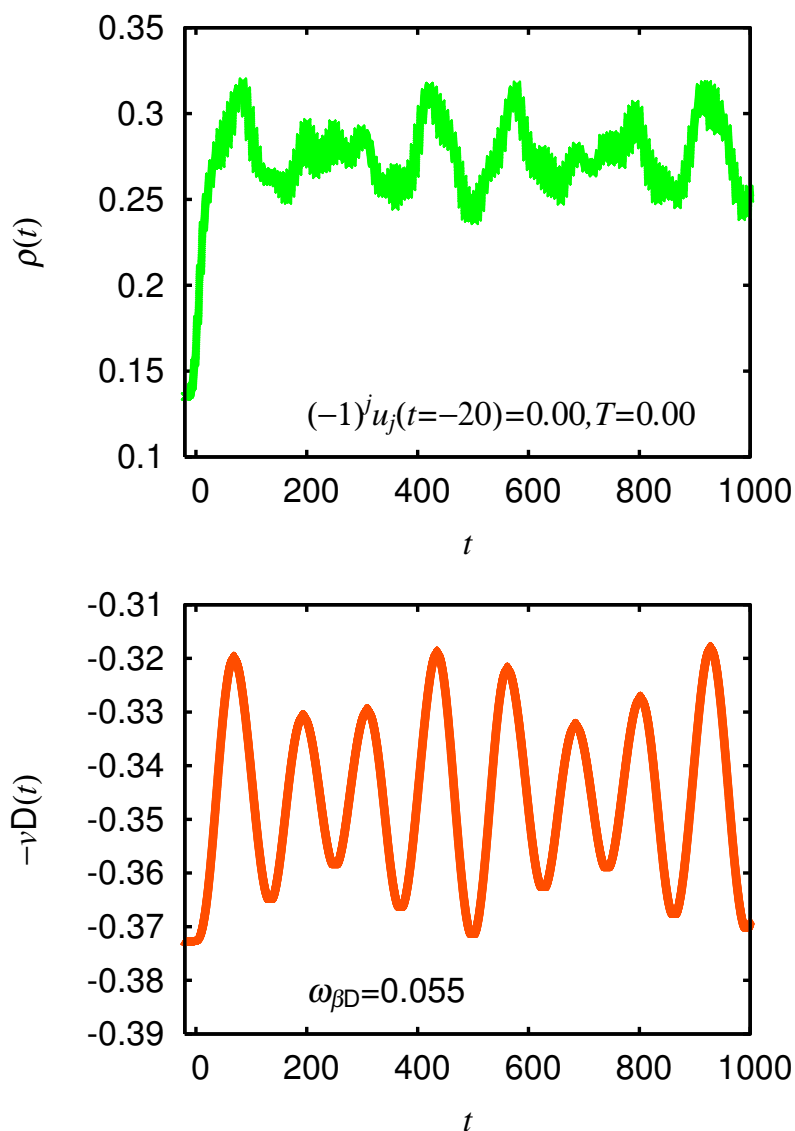

It is shown that, as λ_β increases, the neutral phase is stabilized, and the discontinuity in ionicity is enlarged, by increasing (decreasing) the ionicity in the ionic (neutral) phase on the small-Δ (large-Δ) side of the phase boundary. As a consequence, in order for the ionic phase to be a typical Mott insulator with nearly one electron per site, λ_β should be so large that the neutral phase is sufficiently stabilized. It is evident that, as λ_α increases, the ionic phase is stabilized, and the discontinuity at the transition is suppressed. A finite λ_α is necessary for dimerization and the three-dimensional ferroelectric order with a broken inversion symmetry. Both λ_α and λ_β are large in TTF-CA.

In the case of a large λ_α and a large λ_β, the neutral phase near the phase boundary is photoexcited with an energy just above the optical gap. The time evolution of the ionicity $\rho(t)$ during and after photoexcitation is plotted in Figure 3. In this particular case, the phase boundary is located between

$\Delta = 0.218$ (ionic) and $\Delta = 0.219$ (neutral), and we use $\Delta = 0.219$. For comparison, the displacement on the donor molecule $-v_{\text{D}}(t)$ is also shown.

> **Figure 3.** Transient ionicity $\rho(t)$ (upper) and displacement $-v_{\text{D}}(t)$ with bare energy $\omega_{\beta\text{D}} = 0.055$ (lower) during and after charge-transfer photoexcitation of neutral phase using $\omega_{\text{pmp}} = 0.65$, $T_{\text{pmp}} = 10$, and $F = 1.4$ in case of strong Peierls and Holstein couplings $\lambda_\alpha = 0.167$ and $\lambda_\beta = 0.20$ From [28]. Reproduced with permission from JPSJ.

As $\rho(t)$ increases, the electron density increases for the acceptor molecule and decreases for the donor molecule, so that the displacement increases at the acceptor molecule and decreases at the donor molecule. Thus, $-v_{\text{D}}(t)$ basically behaves as (-1) times the cosine function. The ionicity $\rho(t)$ receives a positive feedback from molecular displacements and oscillates in the same phase with them. This $-$cosine behavior is consistent with the experimental observation [27].

There is a difference between the time profile in Figure 3 and that reported in [27]. If we start from the neutral ground state without short-range lattice dimerization as a precursor, the lattice oscillation grows very gradually (not shown) after photoexcitation that breaks inversion symmetry. However,

the experiment shows a quick growth and oscillation of the lattice dimerization. If we start from the neutral ground state with a (small-amplitude) perfect dimerization without thermal fluctuations, an ultrafast charge transfer between neighboring donor and acceptor molecules continues to oscillate without dephasing, which is not realistic. In order to reproduce the time profile reported in [27], we need to include a small amplitude of lattice dimerization to induce a large-amplitude lattice oscillation immediately after photoexcitation. Then, we introduce in the initial state a dimerization $(-1)^j u_j = 0.01$, which is much smaller than $(-1)^j u_j = 0.058$ of the ground state on the ionic side of the phase boundary. In addition, we need to introduce random numbers according to the Boltzmann distribution at a finite temperature of $T = 0.01$ eV in u_j, $v_j^{(m)}$, $\dot{u}_j$, and $\dot{v}_j^{(m)}$ of the initial state. Figure 4 shows the transient ionicity $\rho(t)$, the displacement on the donor molecule $-v_D(t)$, and the spatially averaged dimerization $\langle (-1)^j u_j(t) \rangle$ in such a case.

Figure 4. Transient ionicity $\rho(t)$ (upper), displacement $-v_D(t)$ with bare energy $\omega_{\beta D} = 0.055$ (middle), and dimerization $\langle (-1)^j u_j(t) \rangle$ with bare energy $\omega_\alpha = 0.013$ (lower) after setting initial dimerization $(-1)^j u_j(t = -20) = 0.01$, adding random numbers ($T = 0.01$) to phonon variables as explained in text, and charge-transfer photoexcitation of neutral phase using $\omega_{pmp} = 0.65$, $T_{pmp} = 10$, and $F = 4.2$ in case of strong Peierls and Holstein couplings $\lambda_\alpha = 0.167$ and $\lambda_\beta = 0.20$ From [28]. Reproduced with permission from JPSJ.
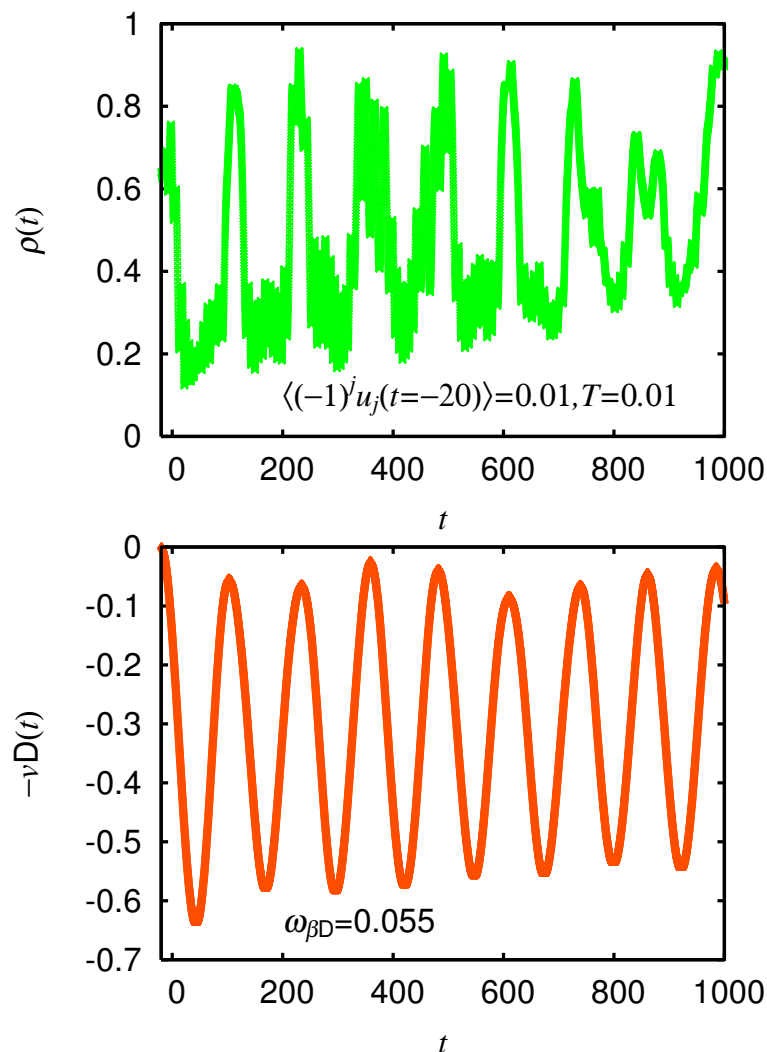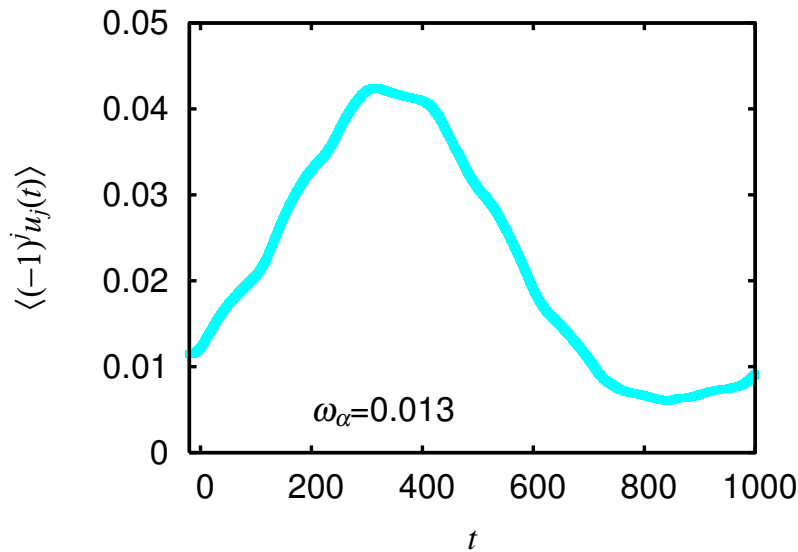
Figure 4. *Cont.*

Now, the phase boundary is located between $\Delta = 0.28$ (ionic) and $\Delta = 0.30$ (neutral), and we use $\Delta = 0.30$. The dimerization $\langle (-1)^j u_j(t) \rangle$ rapidly increases with $\rho(t)$ and oscillates like (-1) times the cosine function. Thus, $\rho(t)$ receives a positive feedback from $\langle (-1)^j u_j \rangle$ already at an early stage as well as from $-v_D(t)$. The amplitude of the $\rho(t)$-oscillation is indeed larger than that without initial dimerization.

In summary, both lattice phonons and molecular vibrations contribute to the thermal and photoinduced neutral-ionic phase transitions. Lattice phonons stabilize the ionic phase through the spin-Peierls mechanism for dimerization and a finite spin gap. Molecular vibrations stabilize the neutral phase through the formation of a bipolaron lattice. The latter produce the large discontinuity in ionicity at the transition. Their contributions are manifested by the photoinduced oscillation of ionicity. The short-range lattice dimerization in the neutral phase promotes the photoinduced growth of a dimerized ionic domain.

3. Melting of Charge Order in θ-Type and α-Type BEDT-TTF Salts

Charge ordering in molecular conductors has been intensively studied both experimentally [40] and theoretically [41]. The Coulomb interaction is a main driving force of charge ordering. It is not due to the Fermi surface nesting, so that it is different from a charge density wave. However, the lattice degrees of freedom must be included in the model to explain the structural deformation at the charge-ordering transition [42,43] and the photoinduced dynamics described below.
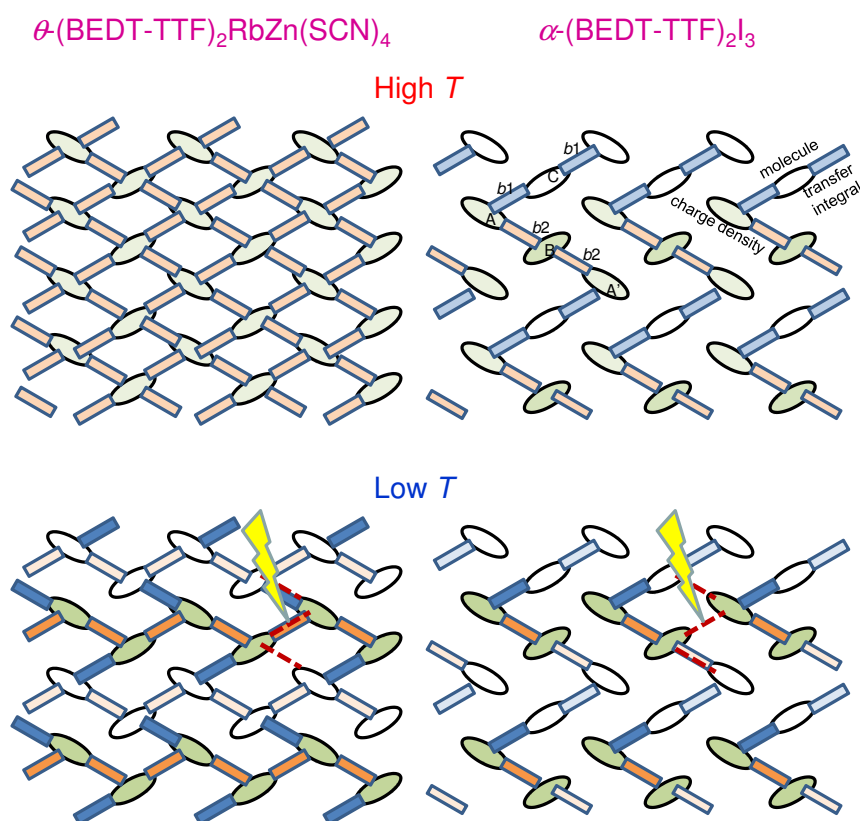
We use the two-dimensional three-quarter-filled extended Peierls–Holstein–Hubbard model

$$H = \sum_{\langle ij \rangle \sigma} (t_{i,j} \pm \alpha_{i,j} u_{i,j})(c_{i\sigma}^\dagger c_{j\sigma} + c_{j\sigma}^\dagger c_{i\sigma}) + U \sum_i n_{i\uparrow} n_{i\downarrow} + \sum_{\langle ij \rangle} V_{i,j} n_i n_j$$
$$+ \sum_{\langle ij \rangle} \frac{K_{i,j}}{2} u_{i,j}^2 + \sum_{\langle ij \rangle} \frac{K_{i,j}}{2\omega_{i,j}^2} \dot{u}_{i,j}^2 + g \sum_i \left(b_i + b_i^\dagger \right) (n_i - 3/2) + \omega_b \sum_i b_i^\dagger b_i \tag{5}$$

where $c_{i\sigma}^\dagger$ creates an electron with spin σ at site i, $n_{i\sigma} = c_{i\sigma}^\dagger c_{i\sigma}$, and $n_i = \sum_\sigma n_{i\sigma}$. The quantity $u_{i,j}$ denotes the intermolecular phonon's displacement, $\dot{u}_{i,j}$ denotes its time derivative, and $b_i^\dagger$ creates a quantum

phonon of energy ω_b, and g is the electron-molecular-vibration coupling strength. The other notations are standard and are introduced in [21]. For instance, $t_{i,j}$ denotes the transfer integral for the bond between the neighboring ith and jth sites. Schematic illustrations of the high- and low-temperature, electronic and lattice structures of the conduction layers in the θ- and α-type salts are shown in Figure 5.

Figure 5. Schematic electronic and lattice structures of θ-(BEDT-TTF)$_2$RbZn(SCN)$_4$ (left) and α-(BEDT-TTF)$_2$I$_3$ (right) at high temperatures (upper) and at low temperatures (lower). The dashed lines in the lower panels indicate local photoexcitations used in the Hartree–Fock calculations.
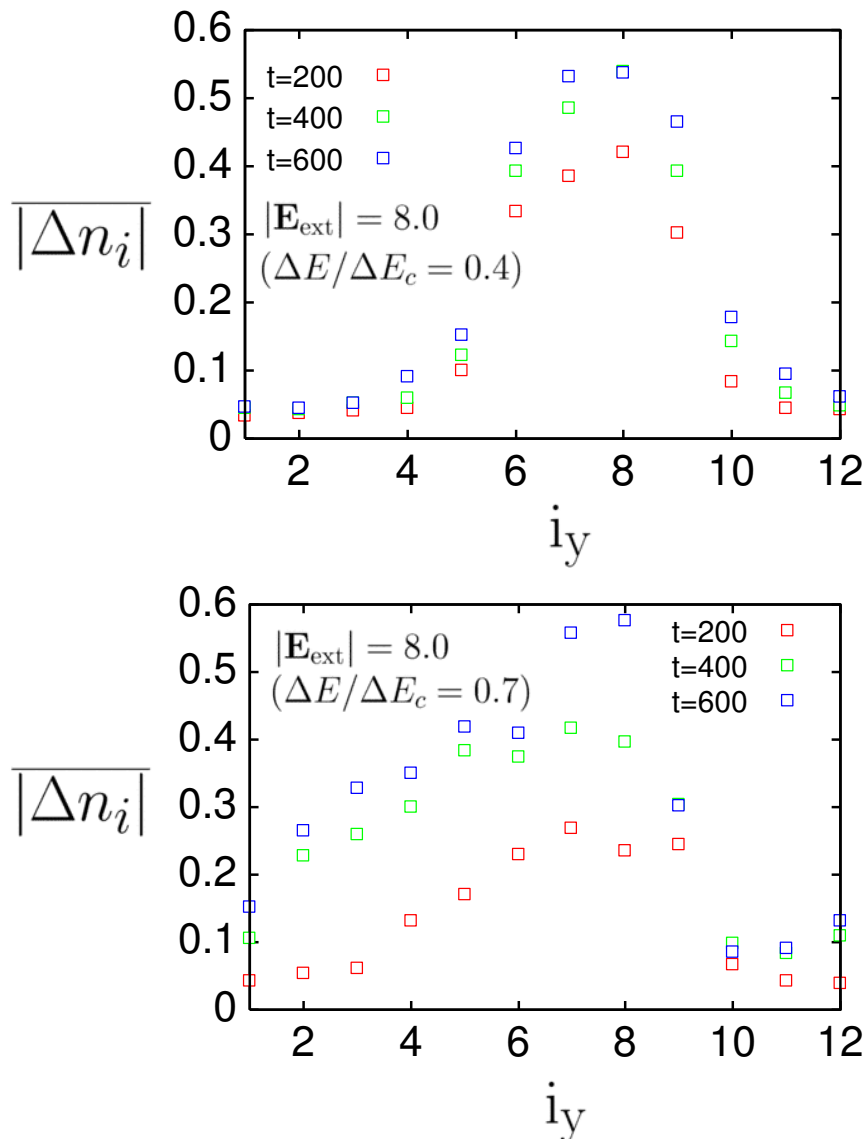

For large systems ($N = 12 \times 12$), we employ the Hartree–Fock approximation for the electronic states and use the parameter values in [20], the results of which are consistent with those for small systems ($N = 12$) with exact many-electron wave functions ($g = 0$) [21]. When we use exact many-electron-phonon wave functions ($g \neq 0$), we use smaller systems ($N = 8$) and the parameter values in [21,22]. Periodic boundary conditions are imposed on all of them. Photoexcitation is introduced in a similar manner to that in the previous section. The time evolution of the wave function and the lattice displacements is obtained by the method described in the previous section.

First, we discuss the different photoinduced melting dynamics of charge orders observed in θ-(BEDT-TTF)$_2$RbZn(SCN)$_4$ and α-(BEDT-TTF)$_2$I$_3$ [19]. For this purpose, we ignore the electron-molecular-vibration coupling by setting $g = 0$ for the moment and use large systems ($N = 12 \times 12$). It is already clarified that the mechanisms for stabilizing the charge orders by lattice distortions are different in these two salts [20]. In θ-(BEDT-TTF)$_2$RbZn(SCN)$_4$, the whole charge-rich (charge-poor) stripe is stabilized by strengthening (weakening) the horizontally connected bonds, as schematically shown in Figure 5. In

α-(BEDT-TTF)$_2$I$_3$, the metallic phase without lattice distortion at high temperatures already possesses a charge-rich site B and a charge-poor site C from the kinetic origin. At low temperatures, the charge-rich site A and the charge-poor site A' bridged by the site B are locally stabilized by lattice distortion. Thus, local photoexcitations would easily weaken the charge order in the latter salt, while the charge order in the former salt would be robust.

Then, we investigate the growth of photoinduced domains with weakened charge order after artificially local photoexcitation as indicated by the dashed lines in the lower panels of Figure 5, by concentrating a finite vector potential on the bonds [(i_x, i_y) = (7.5, 7), (7.5, 7.5), and (7.5, 8)] that connect four sites within a unit cell. Figure 6 shows, in the parenthesis, the ratio $\Delta E / \Delta E_c$, where ΔE is the increment in the total energy per site after local photoexcitation, and ΔE_c is the critical increment above which the charge order is completely melted by global photoexcitation.

Figure 6. i_y dependence of $\overline{|\Delta n_i|}$ at t = 200, 400, and 600 for photoexcitation $F/T_{\mathrm{pmp}} = |\boldsymbol{E}_{\mathrm{ext}}| = 8.0$ along stripes, $\omega_{\mathrm{pmp}} = 0.4$, and $T_{\mathrm{pmp}} = 236$ in case of θ-(BEDT-TTF)$_2$RbZn(SCN)$_4$ (upper) and α-(BEDT-TTF)$_2$I$_3$ (lower), where i_y is coordinate along c-axis (upper) and a-axis (lower) From [20]. Reproduced with permission from JPSJ.
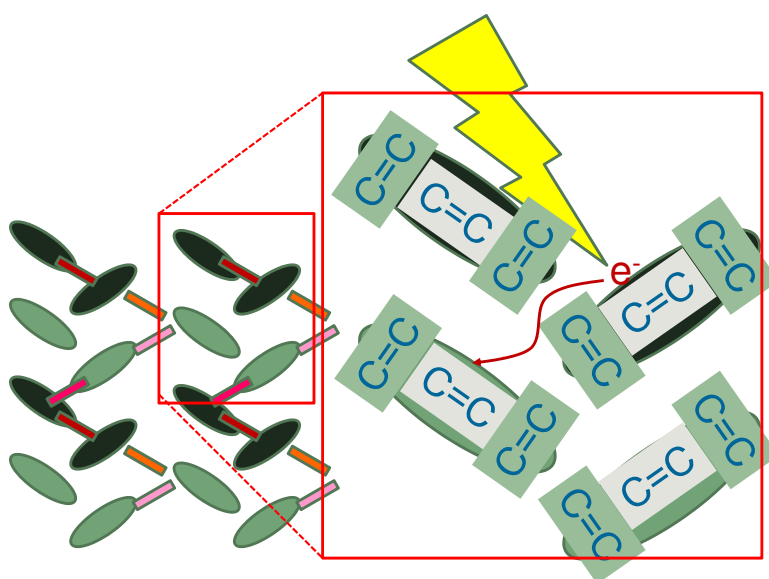
In Figure 6, the absolute values of the differences between the hole densities at $t = 0$ and those at $t = 200$, 400, and 600 are averaged over the direction parallel to the stripes and denoted by $\overline{|\Delta n_i|}$:

$$\overline{|\Delta n_i|} = (1/L_x) \sum_{i_x} |\langle \psi(t) | n_i | \psi(t) \rangle - \langle \psi(0) | n_i | \psi(0) \rangle| \tag{6}$$

where $|\psi(t)\rangle$ is the wave function at time t, $L_x = 12$ is the number of sites along the axis parallel to the stripes, and i_x (i_y) is the coordinate parallel (perpendicular) to the stripes. It gives a measure of how the photoinduced domain grows in the direction perpendicular to the stripes. In θ-(BEDT-TTF)$_2$RbZn(SCN)$_4$, the photoinduced domain remains localized near the place of photoexcitation, and hardly grows to the direction perpendicular to the stripes. This property prevents $\Delta E / \Delta E_c$ from becoming large. For α-(BEDT-TTF)$_2$I$_3$, the photoinduced domain expands to the perpendicular direction. This result suggests that a macroscopic domain is much more easily created in the latter salt than in the former salt.

Next, we consider early-stage dynamics. Photoexcitations transfer electrons between neighboring molecules. Transfer integrals that are responsible for it are typically about 0.2 eV, which correspond to 20 fs in the time domain. Meanwhile, periods of lattice oscillations are typically about 1 ps. Thus, we expect that it takes about 1 ps for the lattice effect to appear in the electronic dynamics. Vibrations that have energy scales comparable with intermolecular transfer integrals are those inside a molecule, e.g., C=C stretching modes. Because these molecular vibrations and lattice phonons are coupled, the lattice effect on the electronic dynamics may appear much earlier than 1 ps through their couplings with molecular vibrations. Nonetheless those vibrations which strongly influence the early-stage electronic dynamics are intramolecular ones [22], as schematically shown in Figure 7 and as demonstrated below.

Figure 7. Schematic electronic and molecular structures of (BEDT-TTF)$_2$X that are relevant to early-stage photoexcited dynamics.
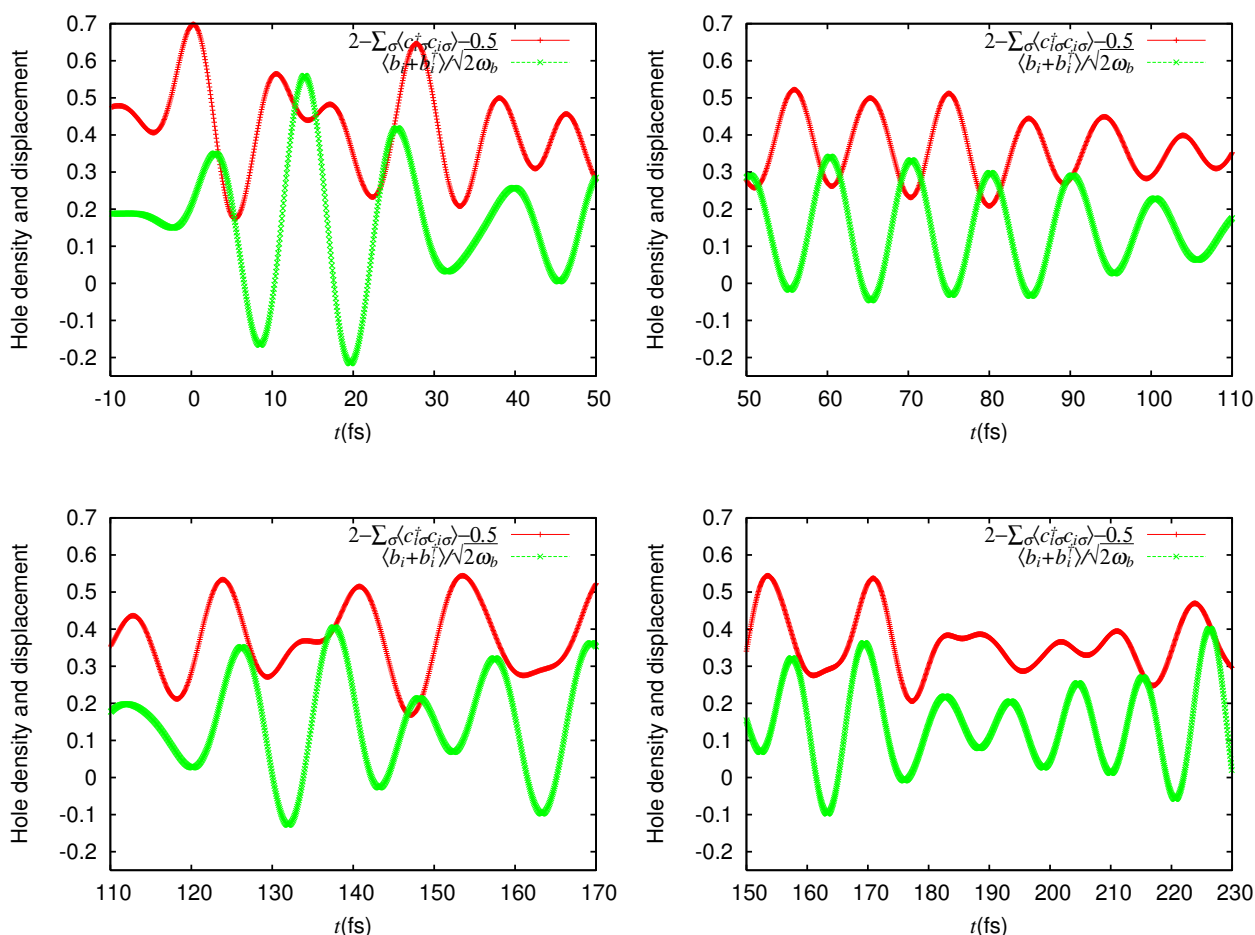

We take an electron-molecular-vibration coupling into account. Because the electronic and vibronic energy scales are comparable, the Born–Oppenheimer approximation breaks down. Thus, we treat molecular vibrations quantum-mechanically (and lattice phonons classically). In numerical calculations,

we compared results when molecular vibrations are quantum-mechanically treated and those when they are classically treated and found large differences especially in the electron-molecular-vibration interference pattern. This is in contrast to the case of the neutral-ionic transition in the previous section, where the transition is from an insulator to another insulator. When they are quantum-mechanically treated, the dimension of the wave function becomes huge. Then, we use a weak coupling ($g = 0.0625$ eV) and a large bare energy for the molecular vibration ($\omega_b = 0.36$ eV), which is comparable with the charge-transfer excitation energy in small systems ($N = 8$).

Figure 8 shows the time evolution of the hole density (red line) and the molecular displacement (green line) at molecule A, where the difference between the equilibrium values at the metal and insulator phases becomes the largest.

Figure 8. Time (in units of femtoseconds) dependence of hole density relative to average value $2 - \sum_\sigma \langle c_{i\sigma}^\dagger c_{i\sigma} \rangle - 0.5$ (red) and molecular displacement $\langle b_i + b_i^\dagger \rangle / \sqrt{2\omega_b}$ (green) at molecule i = A during and after photoexcitation $F = 1$ along stripes, $\omega_{\mathrm{pmp}} = 0.35$, and $T_{\mathrm{pmp}} = 5$ fs in case of α-(BEDT-TTF)$_2$I$_3$ [22].

The four panels sequentially show the evolution, which are separated for the purpose of explanation. Initially (top left panel), the oscillating electric field of pulse width $T_{\mathrm{pmp}} = 5$ fs is applied to the system around $t = 0$. It directly oscillates the hole density. Then, it forces the molecular displacement to oscillate indirectly through the electron-molecular vibration coupling. The sign of the displacement is so chosen

that it becomes large (small) when the hole density is large (small) in equilibrium. Thus, they are initially in phase.
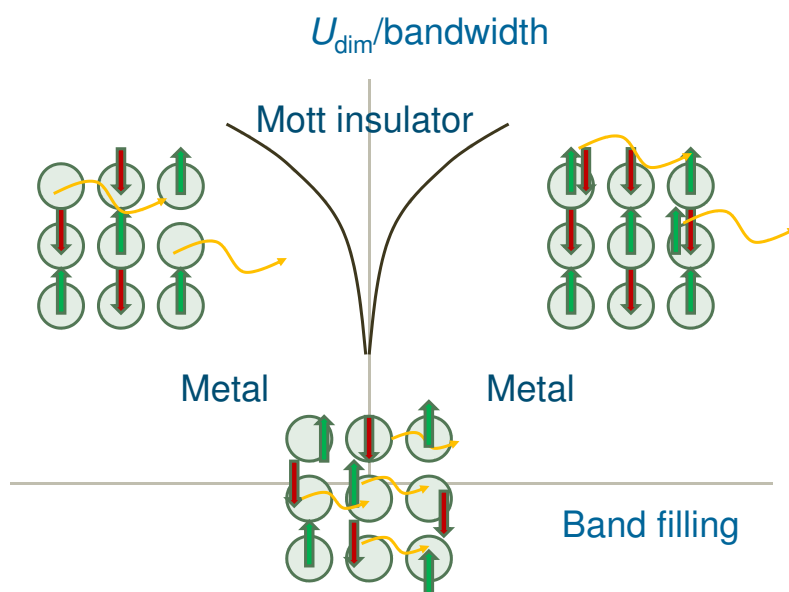
About 50 fs after the photoexcitation (top right panel), they become out of phase. We calculated their dynamics with different parameters and frequently found their out-of-phase motions on this time scale. The energy supplied by the photoexcitation is much larger than the electron-molecular-vibration coupling. It can only partially absorb the energy and consequently makes the motions of the hole density and the molecular displacement out of phase. Soon after this (bottom left panel), their phases become mismatched, and finally (bottom right panel), the hole density follows the molecular displacement, the frequency of which is renormalized by electronic excitations to be smaller than the bare value. These results are consistent with the experimentally observed behavior [22]. In reality, different frequencies of different intramolecular vibrations are coupled, with different strengths, to electrons in the highest occupied molecular orbital, so that the experimentally observed interference pattern is a little more complex.

In summary, both lattice phonons and molecular vibrations contribute to the photoinduced charge-order melting dynamics in the θ-type and α-type BEDT-TTF salts. On the time scale of lattice phonons, the different dynamics in these salts manifest the way by which the charge order is stabilized by lattice phonons is different in these salts. The charge order in the θ-type salt is robust, while that in the α-type salt is fragile. On the time scale of molecular vibrations, *i.e.*, at an early stage, the charge dynamics and the vibrational dynamics interfere with each other. To reproduce the interference pattern theoretically, the quantum nature of molecular vibrations must be properly taken into account.

4. Mott-Insulator-to-Metal Transition in κ-Type BEDT-TTF Salts

Mott insulators are generally converted into metals either by weakening the effective on-site repulsion or by introducing carriers, as schematically shown in Figure 9.
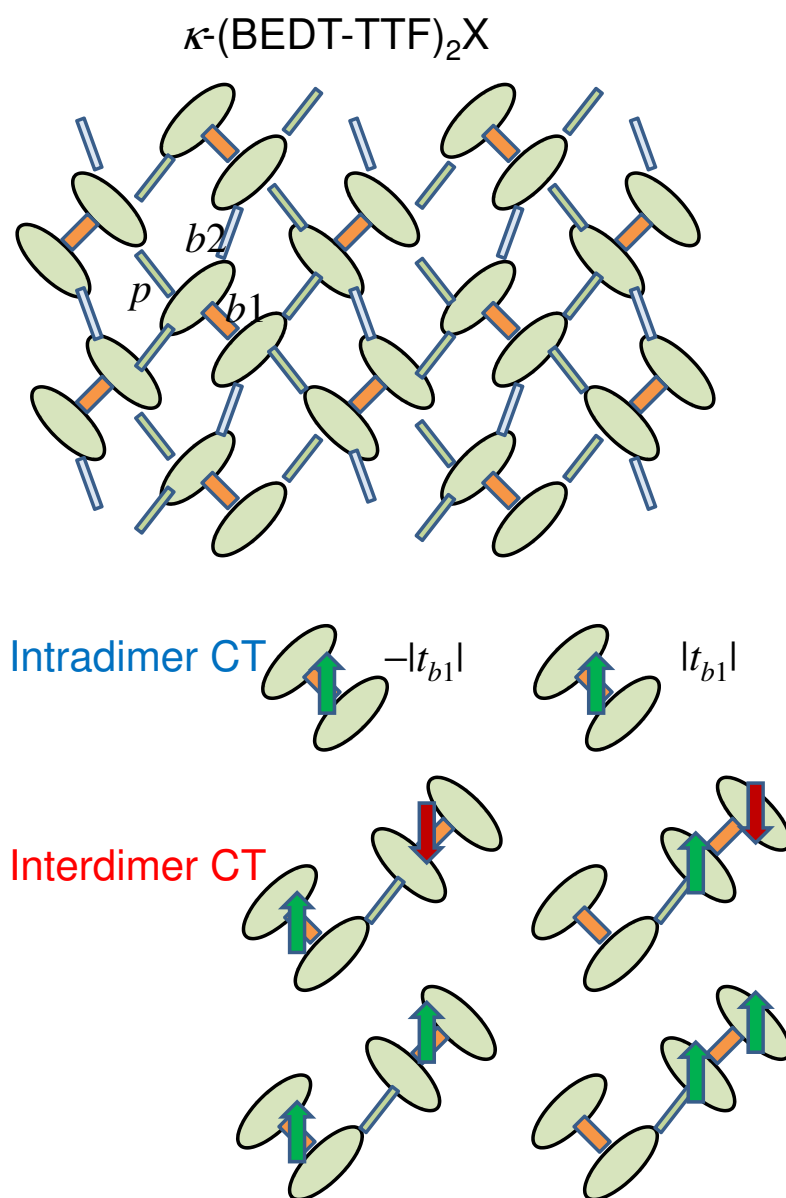
Figure 9. Schematic diagram of Mott insulator and metal phases spanned by effective on-site repulsion (relative to bandwidth) and band filling.

Photoexcitation may be able to induce a Mott-insulator-to-metal transition via one of these pathways. In most situations, it is realized by the introduction of carriers [9,11,12]. Note that carriers introduced by photoexcitations are different from those in a doped Mott insulator in the sense that equal amount of positively charged carriers (empty sites) and negatively charged carriers (doubly occupied sites) are introduced. Their binding through the attractive Coulomb interaction is suppressed by electron correlations, so that the conductivity spectra of photoexcited and doped Mott insulators are similar [10]. Recently, it has been suggested that both pathways are realized by tuning the photoexcitation energy [15]. It uses the intradimer molecular degrees of freedom in a dimer Mott insulator.

We use the two-dimensional three-quarter-filled extended Peierls–Hubbard model on the anisotropic triangular lattice schematically shown in Figure 10.

Figure 10. Schematic electronic and lattice structures of κ-(BEDT-TTF)$_2$X with intradimer and interdimer charge-transfer excitation processes.

$$H = \sum_{\langle ij \rangle \sigma} \left\{ \left[t_{ij}^{(0)} - g_{ij} \left(b_{ij} + b_{ij}^\dagger \right) \right] c_{i\sigma}^\dagger c_{j\sigma} + \text{H.c.} \right\}$$
$$+ U \sum_i n_{i\uparrow} n_{i\downarrow} + \sum_{\langle ij \rangle} V_{ij} n_i n_j + \sum_{\langle ij \rangle} \omega_{ij} b_{ij}^\dagger b_{ij} \tag{7}$$

where $c_{i\sigma}^\dagger$ creates an electron with spin σ at site i, $n_{i\sigma} = c_{i\sigma}^\dagger c_{i\sigma}$, and $n_i = \sum_\sigma n_{i\sigma}$. The operator $b_{ij}^\dagger$ creates a quantum phonon of energy ω_{ij}, and g_{ij} is the electron-phonon coupling strength. The other notations are standard and are introduced in [16]. For instance, the intersite Coulomb repulsion V_{ij} is assumed to be $V_{ij} = V_0/\mid \boldsymbol{r}_i - \boldsymbol{r}_j \mid$ for the neighboring sites i and j at $\boldsymbol{r}_i$ and $\boldsymbol{r}_j$. For simplicity, we consider only one mode for the creation operators $b_{ij}^\dagger$, which modulate the intradimer transfer integrals t_{b1}. Thus, we have $\omega_{ij} = \omega_{b1}$ and $g_{ij} = g_{b1}$. We take a high phonon energy $\omega_{b1} = 0.05$ and a strong electron-phonon coupling $g_{b1} = 0.06$ to make the intradimer and interdimer charge-transfer (CT) bands overlap to a large extent. We use exact many-electron-phonon wave functions on small systems ($N = 8$) with periodic boundary condition and with the number of phonons restricted to a maximum of three at any $b1$ bond, and the parameter values in [16]. Photoexcitation is introduced in a similar manner to that in the previous sections. The time evolution of the wave function is obtained by the method described in the previous sections.
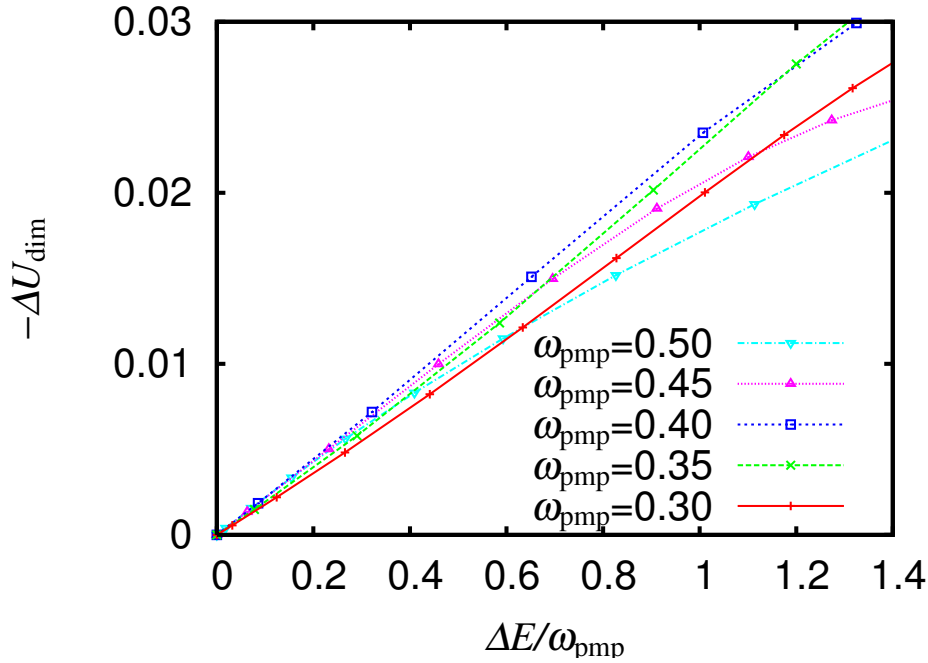
The effective on-site Coulomb energy U_{dim} is evaluated from the energies of the lowest one- and two-hole states for an isolated dimer with a transfer integral t_{b1}, on-site U and intersite V_{b1} repulsion strengths on the molecular bases. It is given by

$$U_{\text{dim}} = \frac{U + V_{b1}}{2} - \sqrt{\left(\frac{U - V_{b1}}{2} \right)^2 + 4t_{b1}^2} + 2 \mid t_{b1} \mid \tag{8}$$

which are modulated by the displacement $\langle b_{b1} + b_{b1}^\dagger \rangle$ through the relation $t_{b1} = t_{b1}^{(0)} - g_{b1} \langle b_{b1} + b_{b1}^\dagger \rangle$. Owing to the molecular degrees of freedom inside a dimer, there are intradimer and interdimer CT excitations, as schematically shown in Figure 10. The force applied to the displacement $\langle b_{b1} + b_{b1}^\dagger \rangle$ depends linearly on the photoinduced difference in the expectation value $\sum_\sigma \langle c_{i\sigma}^\dagger c_{j\sigma} + c_{j\sigma}^\dagger c_{i\sigma} \rangle$ between sites i and j inside the dimer. It is analytically shown that this difference is insensitive to the photoexcitation energy (*i.e.*, whether charge is transferred inside a dimer or between dimers) [16]. As a consequence, any photoexcitation reduces $\sum_\sigma \langle c_{i\sigma}^\dagger c_{j\sigma} + c_{j\sigma}^\dagger c_{i\sigma} \rangle$, reduces the magnitude of the intradimer transfer ($t_{b1} < 0$), and weakens the effective on-site repulsion U_{dim}.

In order to see the modulation of the effective on-site repulsion U_{dim} in a direct manner, we calculate the expectation value of the displacement $\langle b_{ij} + b_{ij}^\dagger \rangle$ as a function of time after photoexcitation. Its maximum decrement, $-\Delta \langle b_{ij} + b_{ij}^\dagger \rangle$, gives the maximum decrement in U_{dim}, $-\Delta U_{\text{dim}}$ through Equation (8). We vary the electric field amplitude F and calculate the increment in the total energy ΔE divided by ω_{pmp}, which corresponds to the number of absorbed photons. We show $-\Delta U_{\text{dim}}$ in Figure 11 as a function of $\Delta E/\omega_{\text{pmp}}$ for different ω_{pmp}.

Figure 11. Modulation of effective on-site repulsion $-\Delta U_{\mathrm{dim}}$, as a function of the number of absorbed photons $\Delta E/\omega_{\mathrm{pmp}}$, for different ω_{pmp} From [16]. Reproduced with permission from JPSJ.

Because the force applied to phonons is similar between the intradimer and interdimer CT processes, the ratio of $-\Delta U_{\mathrm{dim}}$ to $\Delta E/\omega_{\mathrm{pmp}}$ is almost independent of the excitation energy at least in the range of $0.3 < \omega_{\mathrm{pmp}} < 0.5$, which covers the intradimer and interdimer CT excitations. The effective on-site repulsion is therefore confirmed to be weakened to a similar extent irrespective of whether charge is transferred mainly within a dimer or mainly between dimers.

The number of carriers involved in the optical excitations up to ω_{prb} is known to be proportional to the spectral weight obtained by the integration of the conductivity over $0 < \omega < \omega_{\mathrm{prb}}$ below the charge gap. We calculate the increment in the conductivity $\Delta\sigma'(\omega_{\mathrm{prb}}, t) = \sigma'(\omega_{\mathrm{prb}}, t) - \sigma'(\omega_{\mathrm{prb}}, -150)$, where

$$\sigma'(\omega_{\mathrm{prb}}, t) = -\frac{1}{N\omega_{\mathrm{prb}}}\mathrm{Im}\langle\psi(t) \mid \boldsymbol{j}\frac{1}{\omega_{\mathrm{prb}} + i\epsilon + E - H}\boldsymbol{j} \mid \psi(t)\rangle \tag{9}$$
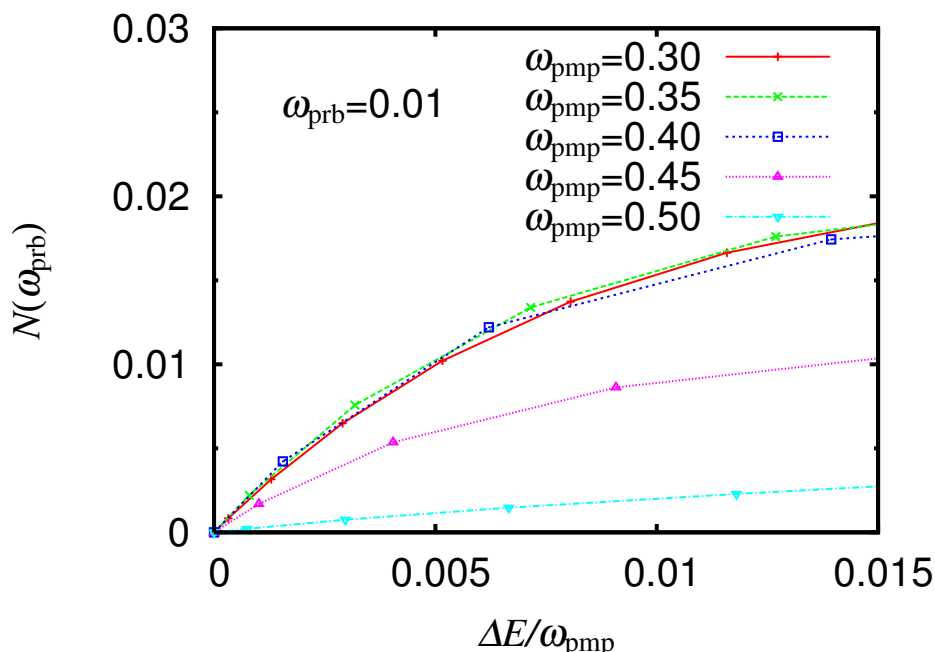
with $\boldsymbol{j}$ being the current operator, ϵ a peak-broadening parameter set at 0.005, and $E = \langle\psi(t) \mid H \mid \psi(t)\rangle$. It is averaged over $150 < t < 750$, $\Delta\sigma'(\omega_{\mathrm{prb}}) = (1/600)\int_{150}^{750}\Delta\sigma'(\omega_{\mathrm{prb}}, t)dt$, and integrated over $0 < \omega < \omega_{\mathrm{prb}}$,

$$N(\omega_{\mathrm{prb}}) = \int_0^{\omega_{\mathrm{prb}}}\Delta\sigma'(\omega)d\omega \tag{10}$$

Figure 12 shows $N(\omega_{\mathrm{prb}})$, as a function of $\Delta E/\omega_{\mathrm{pmp}}$ for different ω_{pmp}.

The energy ω_{prb} is set at 0.01, which is well below the charge gap of 0.18 in the ground state. Although the quantity $N(\omega_{\mathrm{prb}})$ increases with $\Delta E/\omega_{\mathrm{pmp}}$ for any ω_{pmp}, its rate depends largely on ω_{pmp}. For any ω_{prb} below the charge gap, $N(\omega_{\mathrm{prb}})$ increases rapidly for $\omega_{\mathrm{pmp}} = 0.3$, 0.35, and 0.4 and very slowly for $\omega_{\mathrm{pmp}} = 0.5$. For $\omega_{\mathrm{pmp}} = 0.3$, 0.35, and 0.4, the rates are close to each other. The number of carriers involved in the low-energy optical excitations is increased efficiently by $0.3 < \omega_{\mathrm{pmp}} < 0.4$, but it is negligibly increased for $\omega_{\mathrm{pmp}} = 0.5$.

Figure 12. Increment in conductivity time-averaged and integrated over $0 < \omega < \omega_{prb}$, $N(\omega_{prb} = 0.01)$, as a function of the number of absorbed photons $\Delta E/\omega_{pmp}$, for different ω_{pmp} From [16]. Reproduced with permission from JPSJ.

This result shows that carriers introduced by photoexcitations with ω_{pmp} near 0.3 have low excitation energies and are regarded as delocalized. These excitations are characterized as interdimer CT excitations. Although any CT excitation weakens U_{dim}, it requires lattice motion and a long time. Consequently, if a Mott-insulator-to-metal transition is induced, it is mainly through the introduction of carriers. A photoexcitation with $\omega_{pmp} = 0.5$ introduces a negligible number of carriers. As a consequence, if a Mott-insulator-to-metal transition is induced, it is mainly through the weakening of U_{dim}. This excitation is characterized as an intradimer CT excitation.

In summary, phonons modulating the transfer integral inside a dimer contribute to the realization of different transition pathways from the Mott insulator to the metal. In general, this metal-insulator transition can be induced by the weakening of effective interaction relative to the bandwidth or the introduction of carriers away from half filling. The phonons contribute to the weakening of the interaction irrespective of the photoexcitation energy, but this process is slow. The introduction of carriers is fast, but it strongly depends on the photoexcitation energy.

5. Conclusions

The research field of photoinduced phase transitions is developing rapidly. It is realized by the integration of the development of good target materials, the progress in experimental techniques including the improvement in time resolution of pump-probe spectroscopy, and that in theoretical calculations based on itinerant electron models. A single approach cannot generally cover different time scales of photoinduced dynamics in molecular conductors, where electrons and phonons are strongly correlated and their correlation effects appear differently on respective time scales. Theoretical works

need to link closely with experimental studies on different probes with respective time scales, on which the relevant degrees of freedom depend.

Ideally speaking, it is desirable to have a continuous description from early-stage dynamics of individual motions of electrons and phonons to their collective motions, leading to a phase transition and relaxation to the initial phase. It may make it possible for us to construct an efficient transition pathway from the deterministic quantum regime to the stochastic classical regime. The situation is not so simple at present and possibly forever. It is very hard to approach such systems under nonequilibrium environments. In order to expand the possibilities for optical control of electronic phases, however, we need to clarify dynamical characteristics of quantum many-body systems. One of ultimate goals would be coherent control of photoinduced phase transitions.

For instance, electronic motion would generally interfere with various vibrations at an early stage, so that its effects on later dynamics or a possibility for making the transition more efficient should be pursued. In this context, a link between different hierarchies with respective time scales is one of the most important issues. Molecular materials naturally possess hierarchies, *i.e.*, there exist intra- and inter-molecular degrees of freedom. So far, intermolecular degrees of freedom have mainly been focused. Photoinduced phase transitions proceeding on intra- and inter-molecular, electronic and structural stages will become important issues in the near future. From this viewpoint, the photoinduced dynamics in Pd(dmit)$_2$ metal complexes are currently studied [44].

The difficulty in understanding photoinduced dynamics comes from strong correlations between electrons and phonons. Nonetheless, its possibility for rich phenomena also comes from these strong correlations. Interplay between intra- and inter-molecular degrees of freedom and interplay among correlated electrons, lattice phonons and molecular vibrations will provide key points for developing photoinduced phase transitions in molecular conductors.

Acknowledgements

References

1. Jérome, D. The physics of organic superconductors. *Science* **1991**, *252*, 1509–1514.
2. Kishine, J.; Yonemitsu, K. Dimensional crossovers and phase transitions in strongly correlated low-dimensional electron systems: Renormalization-group study. *Int. J. Mod. Phys. B* **2002**, *16*, 711–771.

3.   Itoi, M.; Araki, C.; Hedo, M.; Uwatoko, Y.; Nakamura, T. Anomalously wide superconducting phase of one-dimensional organic conductor $(TMTTF)_2SbF_6$. *J. Phys. Soc. Jpn.* **2008**, *77*, doi: 10.1143/JPSJ.77.023701.

4.   Kagawa, F.; Itou, T.; Miyagawa, K.; Kanoda, K. Magnetic-field-induced Mott transition in a quasi-two-dimensional organic conductor. *Phys. Rev. Lett.* **2004**, *93*, 127001:1–127001:4.

5.   Kurosaki, Y.; Shimizu, Y.; Miyagawa, K.; Kanoda, K.; Saito, G. Mott transition from a spin liquid to a Fermi liquid in the spin-frustrated organic conductor κ-$(ET)_2Cu_2(CN)_3$. *Phys. Rev. Lett.* **2005**, *95*, 177001:1–177001:4.

6.   Yonemitsu, K.; Nasu, K. Theory of photoinduced phase transitions. *J. Phys. Soc. Jpn.* **2006**, *75*, doi: 10.1143/JPSJ.75.011008.

7.   Yonemitsu, K.; Nasu, K. Theory of photoinduced phase transitions in itinerant electron systems. *Phys. Rep.* **2008**, *465*, 1–60.

8.   Yonemitsu, K. Theory of Photoinduced Phase Transitions in Quasi-One-Dimensional Organic Conductors. In *Molecular Electronic and Related Materials—Control and Probe with Light*; Naito, T., Ed.; Transworld Research Network: Trivandrum, India, 2010; pp. 305–320.

9.   Iwai, S.; Ono, M.; Maeda, A.; Matsuzaki, H.; Kishida, H.; Okamoto, H.; Tokura, Y. Ultrafast optical switching to a metallic state by photoinduced Mott transition in a halogen-bridged nickel-chain compound. *Phys. Rev. Lett.* **2003**, *91*, 057401:1–057401:4.

10. Maeshima, N.; Yonemitsu, K. Photoinduced metallic properties of one-dimensional strongly correlated electron systems. *J. Phys. Soc. Jpn.* **2005**, *74*, 2671:1–2671:4.

11. Okamoto, H.; Matsuzaki, H.; Wakabayashi, T.; Takahashi, Y.; Hasegawa, T. Photoinduced metallic state mediated by spin-charge separation in a one-dimensional organic Mott insulator. *Phys. Rev. Lett.* **2007**, *98*, 037401:1–037401:4.

12. Uemura, H.; Matsuzaki, H.; Takahashi, Y.; Hasegawa, T.; Okamoto, H. Ultrafast charge dynamics in one-dimensional organic Mott insulators. *J. Phys. Soc. Jpn.* **2008**, *77*, doi: 10.1143/JPSJ.77.113714.

13. Yonemitsu, K.; Maeshima, N. Coupling-dependent rate of energy transfer from photoexcited Mott insulators to lattice vibrations. *Phys. Rev. B* **2009**, *79*, 125118:1–125118:6.

14. Segawa, M.; Takahashi, A.; Gomi, H.; Aihara, M. Auger recombination of photogenerated charges in one-dimensional Mott insulators. *J. Phys. Soc. Jpn.* **2011**, *80*, 084721:1–084721:10.

15. Kawakami, Y.; Iwai, S.; Fukatsu, T.; Miura, M.; Yoneyama, N.; Sasaki, T.; Kobayashi, N. Optical modulation of effective on-site Coulomb energy for the Mott transition in an organic dimer insulator. *Phys. Rev. Lett.* **2009**, *103*, 066403:1–066403:4.

16. Yonemitsu, K.; Miyashita, S.; Maeshima, N. Photoexcitation-energy-dependent transition pathways from a dimer Mott insulator to a metal. *J. Phys. Soc. Jpn.* **2011**, *80*, 084710:1–084710:14.

17. Chollet, M.; Guerin, L.; Uchida, N.; Fukaya, S.; Shimoda, H.; Ishikawa, T.; Matsuda, K.; Hasegawa, T.; Ota, A.; Yamochi, H.; Saito, G.; Tazaki, R.; Adachi, S.; Koshihara, S. Gigantic photoresponse in 1/4-filled-band organic salt $(EDO-TTF)_2PF_6$. *Science* **2005**, *307*, 86–89.

18. Onda, K.; Ogihara, S.; Yonemitsu, K.; Maeshima, N.; Ishikawa, T.; Okimoto, Y.; Shao, X.; Nakano, Y.; Yamochi, H.; Saito, G.; Koshihara, S. Photoinduced change in the charge order pattern

in the quarter-filled organic conductor (EDO-TTF)$_2$PF$_6$ with a strong electron-phonon interaction. *Phys. Rev. Lett.* **2008**, *101*, 067403:1–067403:4.

19. Iwai, S.; Yamamoto, K.; Kashiwazaki, A.; Hiramatsu, F.; Nakaya, H.; Kawakami, Y.; Yakushi, K.; Okamoto, H.; Mori, H.; Nishio, Y. Photoinduced melting of a stripe-type charge-order and metallic domain formation in a layered BEDT-TTF-based organic salt. *Phys. Rev. Lett.* **2007**, *98*, 097402:1–097402:4.

20. Tanaka, Y.; Yonemitsu, K. Growth dynamics of photoinduced domains in two-dimensional charge-ordered conductors depending on stabilization mechanisms. *J. Phys. Soc. Jpn.* **2010**, *79*, 024712:1–024712:9.

21. Miyashita, S.; Tanaka, Y.; Iwai, S.; Yonemitsu, K. Charge, lattice, and spin dynamics in photoinduced phase transitions from charge-ordered insulator to metal in quasi-two-dimensional organic conductors. *J. Phys. Soc. Jpn.* **2010**, *79*, 034708:1–034708:10.

22. Kawakami, Y.; Fukatsu, T.; Sakurai, Y.; Unno, H.; Itoh, H.; Iwai, S.; Sasaki, T.; Yamamoto, K.; Yakushi, K.; Yonemitsu, K. Early-stage dynamics of light-matter interaction leading to the insulator-to-metal transition in a charge ordered organic crystal. *Phys. Rev. Lett.* **2010**, *105*, 246402:1–246402:4.

23. Matsuzaki, H.; Matsuoka, T.; Kishida, H.; Takizawa, K.; Miyasaka, H.; Sugiura, K.; Yamashita, M.; Okamoto, H. Novel optical and magnetic bistability and photoinduced transition in a one-dimensional halogen-bridged binuclear Pt complex. *Phys. Rev. Lett.* **2003**, *90*, 046401:1–046401:4.

24. Yonemitsu, K.; Miyashita, N. Coherence recovery and photoinduced phase transitions in one-dimensional halogen-bridged binuclear platinum complexes. *Phys. Rev. B* **2003**, *68*, 075113:1–075113:9.

25. Okamoto, H.; Ishige, Y.; Tanaka, S.; Kishida, H.; Iwai, S.; Tokura, Y. Photoinduced phase transition in tetrathiafulvalene-*p*-chloranil observed in femtosecond reflection spectroscopy. *Phys. Rev. B* **2004**, *70*, 165202:1–165202:18.

26. Yonemitsu, K. Interchain coupling effects on photoinduced phase transitions between neutral and ionic phases in an extended Hubbard model with alternating potentials and an electron-lattice coupling. *Phys. Rev. B* **2006**, *73*, 155120:1–155120:7.

27. Uemura, H.; Okamoto, H. Direct detection of the ultrafast response of charges and molecules in the photoinduced neutral-to-ionic transition of the organic tetrathiafulvalene-*p*-chloranil solid. *Phys. Rev. Lett.* **2010**, *105*, 258302:1–258302:4.

28. Yonemitsu, K. Effects of lattice and molecular phonons on photoinduced neutral-to-ionic transition dynamics in tetrathiafulvalene-*p*-chloranil. *J. Phys. Soc. Jpn.* **2011**, *80*, 084707:1–084707:9.

29. Okamoto, H.; Ikegami, K.; Wakabayashi, T.; Ishige, Y.; Togo, J.; Kishida, H.; Matsuzaki, H. Ultrafast photoinduced melting of a spin-Peierls phase in an organic charge-transfer compound, K-tetracyanoquinodimethane. *Phys. Rev. Lett.* **2006**, *96*, 037405:1–037405:4.

30. Maeshima, N.; Yonemitsu, K. Dynamics of photoexcited states in one-dimensional dimerized Mott insulators. *Phys. Rev. B* **2006**, *74*, 155105:1–155105:11.

31. Maeshima, N.; Yonemitsu, K. Charge-transfer excitations in one-dimensional dimerized Mott insulators. *J. Phys. Soc. Jpn.* **2007**, *76*, 074713:1–074713:6.

32. Maeshima, N.; Yonemitsu, K. Polaronic states with spin-charge-coupled excitation in a one-dimensional dimerized Mott insulator K-TCNQ. *J. Phys. Soc. Jpn.* **2008**, *77*, 074713:1–074713:6.

33. Inoue, H.; Yonemitsu, K. Relaxation process in the photoinduced neutral-ionic paraelectric-ferroelectric phase transition in tetrathiafulvalene-p-chloranil. *Phys. Rev. B* **2007**, *75*, 235125:1–235125:13.

34. Nagaosa, N. Theory of neutral-ionic transition in organic crystals. III. Effect of the electron-lattice interaction. *J. Phys. Soc. Jpn.* **1986**, *55*, doi: 10.1143/JPSJ.55.2754.

35. Iizuka-Sakano, T.; Toyozawa, Y. The role of long-range Coulomb interaction in the neutral-to-ionic transition of quasi-one-dimensional charge transfer compounds. *J. Phys. Soc. Jpn.* **1996**, *65*, doi: 10.1143/JPSJ.65.671.

36. del Freo, L.; Painelli, A.; Soos, Z.G. Giant infrared intensity of the Peierls mode at the neutral-ionic phase transition. *Phys. Rev. Lett.* **2002**, *89*, 027402:1–027402:4.

37. Yonemitsu, K. Lattice and magnetic instabilities near the neutral-ionic phase transition of the one-dimensional extended Hubbard model with alternating potentials in the thermodynamic limit. *Phys. Rev. B* **2002**, *65*, 205105:1–205105:8.

38. Yonemitsu, K. Phase transition in a one-dimensional extended Peierls-Hubbard model with a pulse of oscillating electric field: II. Linear behavior in neutral-to-ionic transition. *J. Phys. Soc. Jpn.* **2004**, *73*, 2879:1–2879:17.

39. Iwai, S.; Tanaka, S.; Fujinuma, K.; Kishida, H.; Okamoto, H.; Tokura, Y. Ultrafast optical switching from an ionic to a neutral state in tetrathiafulvalene-p-chloranil (TTF-CA) observed in femtosecond reflection spectroscopy. *Phys. Rev. Lett.* **2002**, *88*, 057402:1–057402:4.

40. Takahashi, T.; Nogami, Y.; Yakushi, K. Charge ordering in organic conductors. *J. Phys. Soc. Jpn.* **2006**, *75*, doi: 10.1143/JPSJ.75.051008.

41. Seo, H.; Merino, J.; Yoshioka, H.; Ogata, M. Theoretical aspects of charge ordering in molecular conductors. *J. Phys. Soc. Jpn.* **2006**, *75*, 051009:1–051009:21.

42. Tanaka, Y.; Yonemitsu, K. Charge order with structural distortion in organic conductors: Comparison between θ-(ET)$_2$RbZn(SCN)$_4$ and α-(ET)$_2$I$_3$. *J. Phys. Soc. Jpn.* **2008**, *77*, 034708:1–034708:10.

43. Miyashita, S.; Yonemitsu, K. Spin and charge fluctuations and lattice effects on charge ordering in α-(BEDT-TTF)$_2$I$_3$. *J. Phys. Soc. Jpn.* **2008**, *77*, doi: 10.1143/JPSJ.77.094712.

44. Nishioka, K.; Yonemitsu, K. Theory of photoinduced melting of charge order in Et$_2$Me$_2$Sb[Pd(dmit)$_2$]$_2$. *Phys. Status Solidi C* **2012**, in press.